UCRL-JC-127475
PREPRINT

A Three-Dimensional Model for Simulating Atmospheric Dispersion of Heavy-Gases Over Complex Terrain

S.T. Chan

This paper was prepared for submittal to the
10th Joint Conference on the
Applications of Air Pollution Meteorology with the Air and Waste Management Association
Phoenix, Arizona
January 11–16, 1998

September 1997

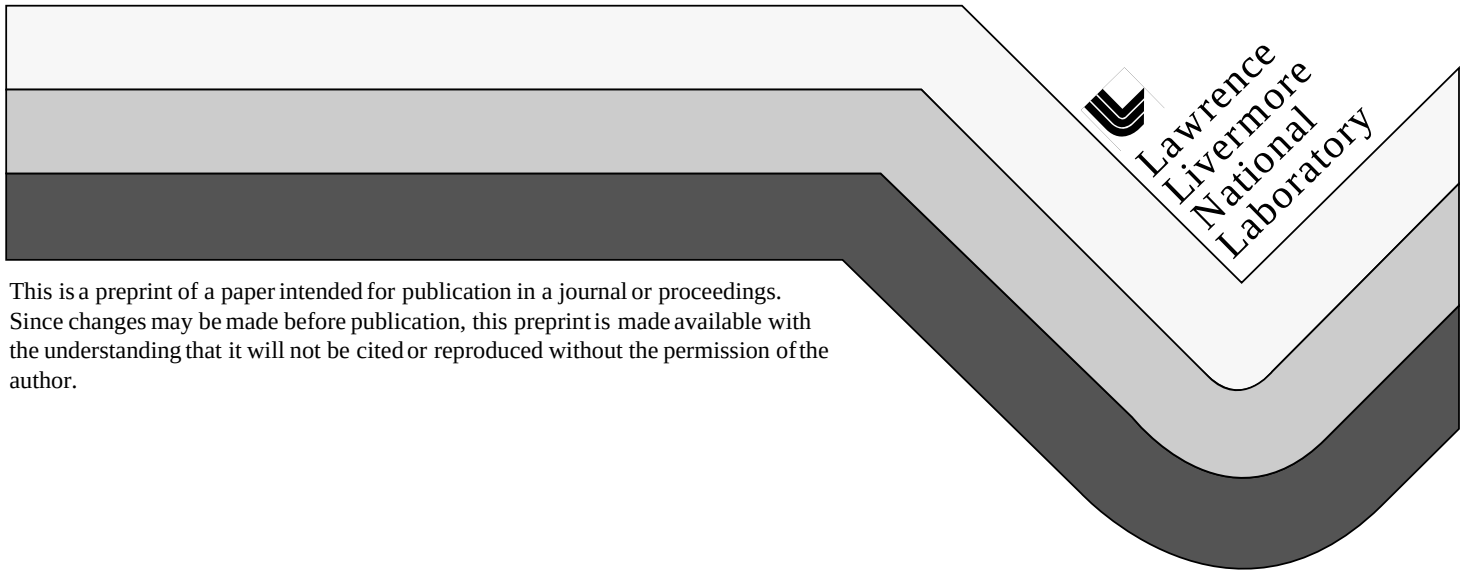

5B.3 A THREE-DIMENSIONAL MODEL FOR SIMULATING ATMOSPHERIC DISPERSION OF HEAVY-GASES OVER COMPLEX TERRAIN

S.T. Chan*
Lawrence Livermore National Laboratory
Livermore, California 94551 USA

1. INTRODUCTION

In recent years there has been significant increase in the industrial use of hazardous gases and liquids. Consequently, increased concern has developed regarding the possibility of accidental releases during the manufacture, storage, transport, or use of these hazardous materials; indeed, accidents have unfortunately occurred and sometimes caused immense damages and casualties. Two of the recent accidents are the tragic methyl isocyanide (MCI) release in Bhopal, India in 1984 which killed 2500 people and the liquefied petroleum gas (LPG) explosions in Mexico City, Mexico, which also happened in 1984 and caused over 400 casualties. Many of the releases produced gas clouds with density heavier than air (also referred to as heavy-gas clouds) owing primarily to one or more of the following factors: high molecular weight, low temperature, and aerosol effects of the released substance.

Heavy-gas releases are generally more hazardous than those involving neutrally or positively buoyant pollutants, since the resulting clouds tend to hug the ground, usually cover greater areas, and persist much longer in time. Their dispersal processes are also more complex to comprehend and predict, because such clouds are closely coupled with the ambient flow and are more profoundly affected by obstacles such as rugged terrain and buildings.

To help understand and simulate the dispersion of such clouds, we have developed a three-dimensional finite element model called FEM3 and an improved version named FEM3A (Chan, 1988) for solving the time-dependent conservation equations based on a generalized anelastic approximation. Such a formulation was employed to permit density changes ($\Delta\rho/\rho_a$) beyond the Boussinesq limits and also to preclude sound waves otherwise present if the fully compressible equations are used. Some of the validation studies can be found in Chan *et al.* (1987) and Chan (1992). More recently, the model has been further enhanced to include the treatment of dispersion scenarios involving density variations much larger than the liquefied natural gas (LNG) range (~0.6) and an advanced turbulence submodel based on the buoyancy-extended $k-\varepsilon$ transport equations (Chan, 1994).

In this paper, the main features of our present model, FEM3C, are briefly described, numerical results from simulations of a field-scale LNG spill experiment are assessed, and a few concluding remarks are made.

* *Corresponding author address*: Stevens T. Chan, Lawrence Livermore National Laboratory P.O. Box 808, L-103, Livermore, CA 94551, e-mail: schan@llnl.gov

2. NUMERICAL MODEL

2.1 Conservation Equations

The following three-dimensional Reynolds-averaged conservation equations, coupled with a turbulence submodel, are solved by the FEM3C model. For brevity, the equations are presented for species in vapor phase only, although FEM3C can also treat a dispersed material in both vapor and droplet phases. The equations, written in Cartesian tensor form, are:

$$\frac{\partial}{\partial t}(\rho u_i) + \rho u_j \frac{\partial u_i}{\partial x_j} = -\frac{\partial p}{\partial x_i} + \frac{\partial}{\partial x_j}(-\rho\overline{u_i' u_j'}) + (\rho - \rho_h) g_i \quad , \tag{1}$$

$$\frac{\partial}{\partial x_j}(\rho u_j) = 0 \quad , \tag{2}$$

$$\frac{\partial \theta}{\partial t} + u_j \frac{\partial \theta}{\partial x_j} = \frac{1}{\rho C_p}\frac{\partial}{\partial x_j}(-\rho C_p \overline{u_j'\theta'}) + \frac{C_{pv} - C_{pa}}{\rho C_p}(-\rho\overline{u_j' q_v'})\frac{\partial \theta}{\partial x_j} \quad , \tag{3}$$

$$\frac{\partial}{\partial t}(\rho q_v) + \rho u_j \frac{\partial q_v}{\partial x_j} = \frac{\partial}{\partial x_j}(-\rho\overline{u_j' q_v'}) \quad , \tag{4}$$

$$\rho = \frac{P M_a}{RT\left[1 + \left(\frac{M_a}{M_v} - 1\right) q_v\right]} \quad , \tag{5}$$

and

$$C_p = C_{pv} q_v + (1 - q_v) C_{pa} \quad . \tag{6}$$

In the above equations, u_i is the i-th component of the mean velocity, θ is the potential temperature deviation from a base state (θ_0), q_v is the mass fraction of species, ρ is the mixture density, p is the pressure deviation from a hydrostatic pressure field (p_h), ρ_h is the density field corresponding to p_h, g_i is the gravitational acceleration, C_p, C_{pa}, and C_{pv} are the specific heats of the mixture, air, and species, $\rho\overline{u_i'u_j'}$, $\rho\overline{u_j'\theta'}$, and $\rho\overline{u_j'q_v'}$ are turbulent fluxes of momentum, energy, and species. M_a and M_v are the molecular weights of air and species, R is the universal gas constant, T is the absolute temperature, and $P = P_h + p$.

The above conservation equations were obtained by generalizing the anelastic approximation of Ogura and Phillips (1962). The essential features of the present conservation equations are that variable density is allowed and sound waves are filtered a priori. The proper interpretation of neglecting $\partial\rho/\partial t$ in the total mass conservation equation is that acoustic density variations in time are assumed to be of very small amplitude and occur so quickly that it is a good approximation to assume density is always in (temporal) equilibrium with the other thermodynamic variables. The time dependence of density is determined implicitly by the time variations of temperature, pressure, and composition via the ideal gas law.

2.2 Turbulence Submodels

In addition to a K-theory submodel (Chan, 1988), we also implemented a slightly modified version of the buoyancy-extended $k-\varepsilon$ model developed by Haroutunia (1987). Assuming a flat terrain, Haroutunia was able to simulate the dense gas dispersion of the Burro-8 LNG field trial conducted by Koopman, *et al.* (1982). However, the simulation failed when the actual irregular topography was accounted for. The failure was considered due to the use of coarse meshes, wall functions, and a geometry-dependent stratification parameter in evaluating the turbulent Prandtl number. Since it is more appropriate to define the turbulent Prandtl number as a function of the flux Richardson number, this approach is taken in the present study. Also an ad-hoc approach is employed in defining the anisotropic property of the eddy viscosity/diffusion tensors. The salient features of our $k-\varepsilon$ submodel are given below. More details can be found in Chan (1994).

The turbulent fluxes are modeled as:

$$-\rho\overline{u_i'u_j'} = \rho K_{ijlm}\left(\frac{\partial u_l}{\partial x_m}+\frac{\partial u_m}{\partial x_l}\right)-\frac{2}{3}\rho k\delta_{ij} \quad , \qquad (7)$$

$$-\rho\overline{u_i'\theta'} = \rho K_{ij}^{\theta}\frac{\partial\theta}{\partial x_j} \quad , \qquad (8)$$

$$-\rho\overline{u_i'q_v'} = \rho K_{ij}^{c}\frac{\partial q_v}{\partial x_j} \quad , \qquad (9)$$

where K_{ijlm}, K_{ij}^{θ}, K_{ij}^{c} are the eddy viscosity/diffusivity tensors for momentum, energy, and species, respectively. These anisotropic diffusion tensors are approximated as:

$$K_{ijlm} \longrightarrow C_\mu\frac{k^2}{\varepsilon}\begin{Bmatrix} 1 & \beta_H & 1 \\ \beta_H & 1 & 1 \\ 1 & 1 & 1 \end{Bmatrix} \quad , \qquad (10)$$

$$\mathrm{P}_{rt}K_{ij}^{\theta} = P_{rt}K_{ij}^{c} = C_\mu\frac{k^2}{\varepsilon}\begin{Bmatrix} \beta_H & 0 & 0 \\ 0 & \beta_H & 0 \\ 0 & 0 & 1 \end{Bmatrix} . \qquad (11)$$

wherein P_{rt} is the turbulent Prandtl number, $C_\mu = 0.09$, and β_H is an input parameter (usually > 1) of the model. Equation (10) is a shorthand notation used to represent the nine non-zero elements of a fourth-order tensor and Eq. (11) is a second-order tensor with non-zero entries for the diagonal terms only. Strictly speaking, the value of β_H should depend on local stability conditions, which are difficult to model accurately. However, for heavy-gas dispersion within the atmospheric boundary, advection transport is usually dominating in the horizontal directions, thus the precise value of β_H is presumably not very crucial in the overall performance of the model.

The turbulent Prandtl number is determined using the following relationship (Ueda *et al.*, 1981),

$$\frac{1}{P_{rt}} = \sigma_{t0}\frac{(1-10R_f)}{(1-R_f)^2} \quad , \qquad (12)$$

in which $\sigma_{to} = 0.9852$ and the flux Richardson number is defined as

$$R_f = -b/s \qquad (13)$$

with b and s being the buoyancy and source terms in the turbulent kinetic energy equation.

The variables k and ε in Eqs. (10) and (11) are obtained from the following transport equations,

$$\frac{\partial}{\partial t}(\rho k) + \rho u_j \frac{\partial k}{\partial x_j} = \frac{\partial}{\partial x_i}\left(\rho K_{ij}^{k} \frac{\partial k}{\partial x_j}\right) + s + b - \rho\varepsilon \ , \qquad (14)$$

$$\frac{\partial}{\partial t}(\rho\varepsilon) + \rho u_j \frac{\partial \varepsilon}{\partial x_j} = \frac{\partial}{\partial x_i}\left(\rho K_{ij}^{\varepsilon} \frac{\partial \varepsilon}{\partial x_j}\right) + C_1\left(\frac{\varepsilon}{k}\right)s + C_1(1-C_3)\left(\frac{\varepsilon}{k}\right)b - C_2\rho\left(\frac{\varepsilon^2}{k}\right) \ , \qquad (15)$$

wherein K_{ij}^{k} and K_{ij}^{ε} are the eddy diffusivity tensors [defined similarly to Eq. (11)] for k and ε respectively. The model constants are: $C_1 = 1.44$, $C_2 = 1.92$, and $C_3 = -0.8$ and 2.15 for the unstable and stable regimes respectively.

2.3 Spatial Discretization and Time Integration

The above set of equations, together with appropriate initial and boundary conditions, are solved to obtain the fields of velocity, pressure, temperature, species, and turbulence quantities. Firstly, the equations are spatially discretized by the finite element techniques (with piecewise constant representation for pressure and trilinear approximations for all other field variables) in conjunction with the Galerkin method of weighted residuals to obtain a coupled system of nonlinear first-order ordinary differential equations. A consistent Poisson equation for pressure is then derived to decouple the velocity and pressure fields. The pressure equation is solved by either a direct method or a preconditioned conjugate gradient solver, and the other field variables are integrated in time using a modified forward Euler method.

3. VALIDATION TESTS

In addition to the test cases of a fully developed channel flow and a turbulent flow over a backward-facing step, the FEM3C model has also been validated against one of the laboratory heavy-gas dispersion experiments investigated by McQuaid (1976). Results from this test are not included here but can be found in Chan (1994).

In the present study, the Burro-8 LNG field dispersion trial, which was conducted under very low wind speed (< 2 m/s) and slightly stable atmospheric conditions by Koopman, *et al.* (1982), is used. During the test, 28.4 m^3 of LNG was spilled (at a rate of 16 m^3/min) onto a water pond, over which the spilled LNG quickly boiled off and formed a heavy-gas cloud. This test is particularly interesting because it is representative of large-scale spills where topography significantly affects the heavy-gas cloud dispersion. The ground topography in the test area is shown in Fig. 1 and the measured concentration contours (in %volume) for two representative planes at $t = 180$ *s* are displayed in Figs. 2 and 3. Due to negative buoyancy and the suppression of turbulence mixing, the resulting vapor cloud is very low and wide, extending well beyond the edges of the instrument array (indicated by the dashed lines). In addition, the vapor cloud is highly bifurcated, with the larger lobe of the cloud shifted towards the lower ground.

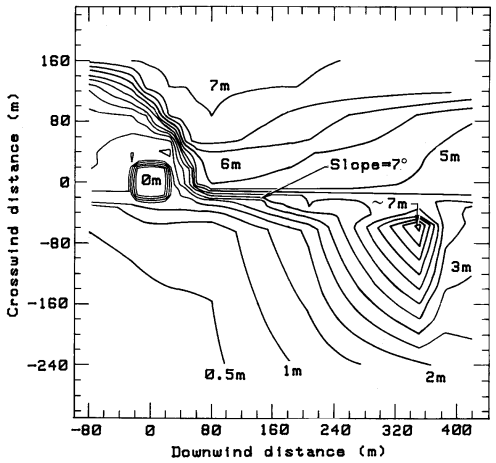

Fig. 1. Topography in the vicinity of the LNG spill facility, China Lake, California.

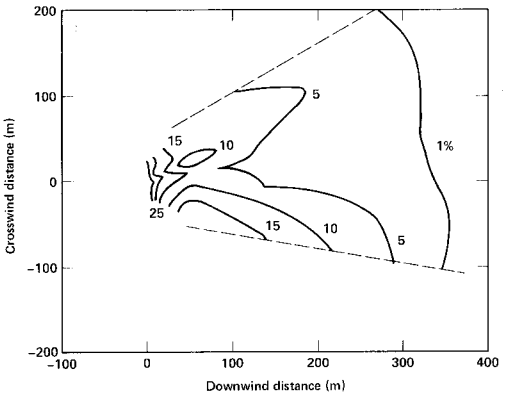

Fig. 2. Measured concentration contours at 1 m height above ground level at $t = 180$ *s*.

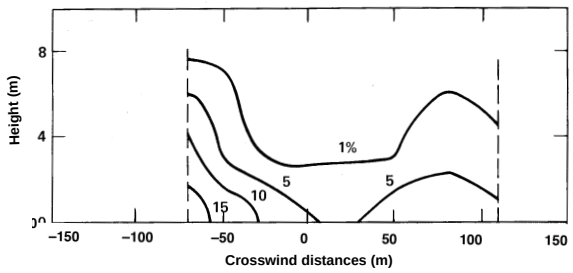

Fig. 3. Measured concentration contours on the crosswind plane at 140 m downwind at $t = 180$ s.

A graded mesh consisting of 42 x 25 x 18 grid points was employed to represent a computational domain of $x = -100$ m to 420 m, $y = -280$ m to 200 m horizontally, and from the ground to $z = 20$ m vertically. The measured data were used to define a logarithmic velocity profile at the inlet plane and appropriate boundary conditions. The spilled LNG was modeled as an evaporating pool of 870 m^2, with a vertical injection velocity of 0.14 m/s for 108 s. For the $k-\varepsilon$ turbulence submodel, wall functions were applied on the ground surface for the momentum equations. For the temperature equation, due to some uncertainties regarding the applicability of the turbulent heat flux formula, which is based on atmospheric boundary layer flow with temperature variations much smaller than those in the present situation, turbulent heat transfer between the ground and the vapor cloud was treated via a bulk heat transfer submodel instead. The test was simulated with both the *K*-theory and the $k-\varepsilon$ turbulence submodels.

In Fig. 4, the predicted concentration contours at 1 m height above ground level at $t = 180$ s are shown. Although both turbulence submodels have produced a wide vapor cloud as observed in the field experiment, the $k-\varepsilon$ turbulence submodel has obviously delivered more accurate results, regarding the shape and size of the vapor cloud, and the bifurcated structure of concentration contours higher than 2%. The concentration contours on the $x = 145$ m crosswind plane for the same time are shown in Fig. 5. Overall, both simulations are able to reproduce a ground-hugging cloud and a shift of the cloud towards the lower terrain. The simulation with the $k-\varepsilon$ submodel, however, has yielded a closer detailed agreement with measurements, regarding the cloud width, the shape of the left lobe, and the presence of higher concentration contours.

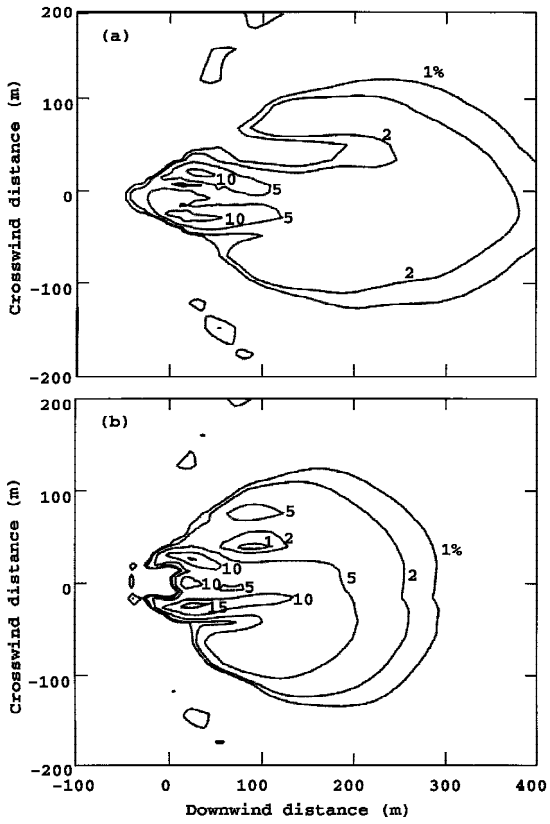

Fig. 4. Calculated concentration contours at 1 m height above ground level at $t = 180$ s: (a) *K*-theory submodel, (b) $k-\varepsilon$ turbulence submodel.

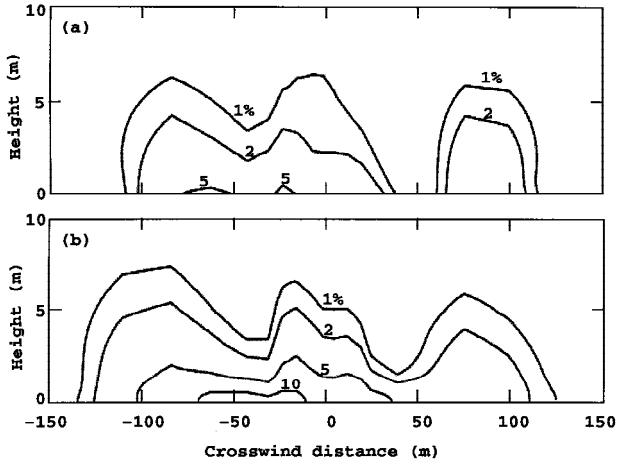

Fig. 5. Calculated concentration contours on the crosswind plane at 145 m downwind at t = 180 s: (a) *K*-theory submodel, (b) $k-\varepsilon$ turbulence submodel.

Results for the maximum concentrations as a function of downwind distance are compared in Fig. 6. In general, values from the *K*-theory submodel agree reasonably well

with the field data except a flatter slope near the end of the curve. On the other hand, the agreement between model predictions and measurements is markedly improved with the $k-\varepsilon$ turbulence submodel, regarding both the magnitude and slope of the curve.

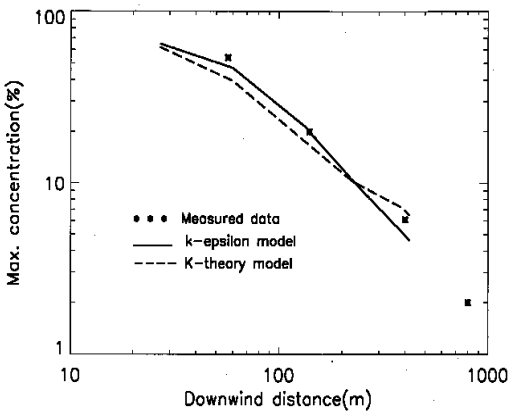

Fig. 6. Calculated and measured maximum concentrations versus downwind distance.

4. CONCLUDING REMARKS

The FEM3C model has been applied to simulate, among others, the dispersion of a field scale heavy-gas cloud, in which gravity flow and terrain effects are important. In general, the FEM3C model is able to reproduce the important cloud features observed in the field experiment, such as a ground-hugging cloud with gravity spread in both horizontal directions, cloud bifurcation, and the shift of the vapor cloud towards the lower terrain. The predicted maximum concentrations in the downwind direction also agree well with field data.

It has been demonstrated that the buoyancy- extended $k-\varepsilon$ turbulence submodel has performed consistently better than the local equilibrium *K*-theory submodel for a dispersion problem wherein gravity flow and terrain effects are important. The improvements can be attributed mostly to the inclusion of transport effects and more realistic length scales used in turbulence parameterization.

While the present model has performed very well for the tests conducted, it can certainly be further improved for more accurate predictions. Some potential areas for improvements are: more accurate treatment of turbulent heat transfer between the ground surface and the vapor cloud and more sophisticated turbulence modeling, for instance, via nonlinear eddy viscosity and without using wall functions.

5. REFERENCES

Chan, S.T., Ermak, D.L., and Morris, L.K., 1987, FEM3 model simulations of selected Thorney Island Phase I Trials. *J. Haz. Mat.*, **16**, 267–292.

Chan, S.T., 1988: FEM3A—A finite element model for the simulation of gas transport and dispersion: User's Manual. UCRL-21043, LLNL, Livermore, CA.

Chan, S.T., 1992: Numerical simulations of LNG vapor dispersion from a fenced storage area. *J. Haz. Mat.*, **30**, 195–224.

Chan, S.T., 1994: Recent upgrades and enhancements of the FEM3A model. UCRL-ID-119749, LLNL, Livermore, CA.

Haroutunian, V., 1987: A time-dependent finite element model for atmospheric dispersion of gases heavier than air, Ph.D. Dissertation, UMIST, U.K.

Koopman, R.P., R.T. Cederwall, D.L. Ermak, H.C. Godwire, Jr., W.J. Hogan, J.W. McClure, T.G. McRae, D.L. Morgan, H.C. Rodean, and J.H. Shinn, 1982: Analysis of Burro Series
40-m^3 LNG Spill Experiments. *J. Haz. Mat.*, **6**, 43–83.

McQuaid, J., 1976: Some experiments on the structure of stably stratified shear flows. Technical Paper P21, Safety in Mines Research Establishment, Sheffield, U.K.

Ogura, Y., and N. Phillips, 1962: Scale analysis of deep and shallow convection in the atmosphere. *J. Atmos. Sci.,* **19**, 173–179.

Ueda, H., S. Mitsumoto, and S. Komori, 1981: Buoyancy effects on the turbulent transport processes in the lower atmosphere. *Quart. J.R. Met. Soc.*, **107**, 561–578.

ACKNOWLEDGMENTS

This work was performed under the auspices of the U.S. Department of Energy by Lawrence Livermore National Laboratory under contract number W-7405-ENG-48.

Technical Information Department • **Lawrence Livermore National Laboratory**
University of California • Livermore, California 94551